Liver-innervating vagal sensory neurons play an indispensable role in the development of hepatic steatosis and anxiety-like behavior in mice fed a high-fat diet.

Jiyeon Hwang[1,2], Junichi Okada[1,2], Jeffrey E. Pessin[1,2,3], Streamson C. Chua Jr.[1,2], Gary J. Schwartz[1,2], and Young-Hwan Jo[1,2,3*]

Affiliations

[1]The Fleischer Institute for Diabetes and Metabolism
[2]Division of Endocrinology, Department of Medicine
[3]Department of Molecular Pharmacology, Albert Einstein College of Medicine, NY, USA

*** Corresponding author: young-hwan.jo@einsteinmed.edu**
Departments of Medicine and Molecular Pharmacology
Albert Einstein College of Medicine,
1300 Morris Park Ave, Bronx, NY 10461
Tel: 718-430-3495

Acknowledgments

General: We thank Dr. Shun-Mei Liu and Licheng Wu for their technical assistance.

Funding: This work was supported by the NIH (R01 AT011653 and R03 TR003313 to Y.-H.J, R01 DK092246 to Y.-H.J and G.J.S., P30 DK020541 to Y.-H.J, G.J.S., and J.E.P. and DK110063 to J.E.P.).

Competing interests: The authors declare no conflict of interest.

Abstract

Background and Aims

The visceral organ-brain axis, mediated by vagal sensory neurons in the vagal nerve ganglion, is essential for maintaining various physiological functions. In this study, we investigated the impact of liver-projecting vagal sensory neurons on energy balance, hepatic steatosis, and anxiety-like behavior in mice under obesogenic conditions.

Methods

We performed single-nucleus RNA sequencing of vagal sensory neurons innervating the liver. Based on our snRNA-Seq results, we used the Avil^{CreERT2} strain to identify vagal sensory neurons that innervate the liver.

Results

A small subset of polymodal sensory neurons innervating the liver was located in the left and right ganglia, projecting centrally to the nucleus of the tractus solitarius, area postrema, and dorsal motor nucleus of the vagus, and peripherally to the periportal areas in the liver. Male and female control mice developed diet-induced obesity (DIO) during high-fat diet feeding. Deleting liver-projecting advillin-positive vagal sensory neurons prevented DIO in male and female mice, and these outcomes are associated with increased energy expenditure. Although males and females exhibited improved glucose homeostasis following disruption of liver-projecting vagal sensory neurons, only male mice displayed increased insulin sensitivity. The loss of liver-projecting vagal sensory neurons limited the progression of hepatic steatosis in male and female mice fed a steatogenic diet. Finally, mice lacking liver-innervating vagal sensory neurons exhibited less anxiety-like behavior compared to the control mice.

Conclusions

The liver-brain axis contributes to the regulation of energy balance, glucose tolerance, hepatic steatosis, and anxiety-like behavior depending on the nutrient status in healthy and obesogenic conditions.

Keywords:

Anxiety, neural circuit, sensory, vagus, fatty liver

Introduction

Communication between the visceral organs and the brain is required to maintain metabolic homeostasis. Vagal sensory neurons present in the vagus nerve ganglia transmit interoceptive signals from visceral organs to the medulla[1]. Each type of vagal sensory neurons with unique molecular features has a specific target organ such as the larynx, stomach, intestine, pancreas, heart, and lung[2-9]. The highly specialized cellular, molecular, and anatomical organization of vagal sensory neurons has been shown to be crucial for the proper detection and integration of interoceptive signals to control metabolic homeostasis and other vital functions, such as breathing and reward[1-10].

The molecular identity of vagal sensory neurons appears to play a major role in determining their functional properties[3-7, 9]. For example, vagal sensory neurons that control the digestive system include vasoactive intestinal peptide-, glucagon-like peptide 1 receptor-, oxytocin receptor-, and G protein-coupled receptor 65-expressing neurons[3, 6]. Interestingly, distinct types of vagal sensory neurons (somatostatin- vs. CGRP-positive cells) innervate different parts of the stomach[3]. Those innervating the lungs are purinergic receptor P2RY1-positive neurons and neuropeptide Y receptor Y2-expressing neurons[4]. Pancreatic islets are innervated by vagal sensory neurons expressing substance P, calcitonin gene-related peptide (CGRP), and 5-HT3 receptors[5]. However, there is limited information available about the molecular identity of vagal sensory neurons that innervate the liver and their role in hepatic metabolism. It appears that only a limited number of vagal sensory neurons in the left nodose ganglion project to the liver in rats[11]. The peripheral nerve terminals of the vagal sensory neurons innervating the liver are primarily present in the bile ducts and portal veins, whereas no afferent terminals are observed in the hepatic parenchyma of rats[12].

The liver is the largest metabolic organ responsible for the body's energy needs and surfeits. As the functions of organs, including the brain, depend largely on the fuel produced by the liver, dysregulation of hepatic metabolism would significantly affect their functions. Although the brain is the most energy-demanding organ in the body, it remains relatively unknown whether hepatic metabolism can influence brain function. In fact, individuals with nonalcoholic fatty liver disease (NAFLD) have a higher risk of psychiatric disorders including anxiety, depression, bipolar disorder, schizophrenia, and dementia[13-15], suggesting that impaired hepatic lipid metabolism may be closely associated with mental illness. As liver-derived

interoceptive signaling molecules can reach higher brain centers via hepatic vagal sensory neurons and humoral pathways, it is reasonable to assume that disrupted interoceptive signaling caused by NAFLD may result in psychiatric illness. In this study, we sought to determine the molecular identity of vagal sensory neurons innervating the liver and their role in controlling hepatic steatosis and anxiety-like behavior.

Materials and Methods

Animals

All mouse care and experimental procedures were approved by the Institutional Animal Care Research Advisory Committee of Albert Einstein College of Medicine.

Eight-nine-week-old Avil^{CreERT2} (stock # 032027) and Rosa26-floxed-STOP-Cas9-eGFP mice (Rosa26-eGFP^{f} , stock# 024857) were purchased from the Jackson Laboratory (see Supplementary Materials and Methods).

Viral injection

We used AAVrg-Cre (Addgene 55636-AAVrg, titer; 2.2 x10^{13} pfu/ml), AAVrg-FLEX-GFP (Addgene 51502-AAVrg, titer; 2.3 x10^{13} pfu/ml), AAVrg-FLEX-jGCamp7s (Addgene 104491, titer; 2.5 x10^{13} pfu/ml). Avil^{CreERT2} mice received a total volume of 20 ul of viral injection into the medial and left lobes of the livers. Mice were killed 5 and 10 weeks post-viral inoculation.

To ablate liver-innervating vagal sensory neurons, a total volume of 20 ul of AAVrg-FLEX-taCasp3-TEVp (titer >1×10^{12} pfu/ml; Addgene 45580) was injected into the medial and left lobes of the livers of Avil^{CreERT2} mice. AAVrg-FLEX-GFP (Addgene 51502-AAVrg, titer > 1×10^{13} pfu/ml) was used as control.

Clear, unobstructed brain imaging cocktails (CUBIC) tissue clearing and immunostaining.

The CUBIC method[16] was used to clear brainstem tissues. Detailed methods were described in Supplementary Materials and Methods.

Immunostaining

Nodose ganglia, liver, and brain were post-fixed in 4% paraformaldehyde overnight in a cold room and then in 30% sucrose the following day. Tissues were sectioned using a cryostat at 16-20 μm (see Supplementary Materials and Methods).

Measurement of body weight, body composition, and blood glucose

Body weight was measured weekly at 9 a.m. Body composition for fat mass and fat-free mass was assessed using the EchoMRI system. Blood samples were collected from the mouse tail, and a small drop of blood was placed on the test strip of a glucose meter.

Assessment of glucose tolerance and insulin tolerance

For the GTT, the experimental and control mice were fasted for 15 h (6:00 pm–9:00 am). Sterile glucose solution was administered intraperitoneally at a concentration of 2 g/kg (glucose/body weight) (see Supplementary Materials and Methods). For the ITT, the mice were fasted for 4 h (see Supplementary Materials and Methods).

Assessment of energy expenditure

Indirect calorimetry was performed for three days at the end of 10 weeks (see Supplementary Materials and Methods).

Reverse transcription-quantitative polymerase chain reaction (RT-qPCR)

Liver tissues were collected from the experimental and control groups–10-12 weeks post viral inoculation. Liver tissues were homogenized in TRIzol reagent (ThermoFisher Scientific, 15596-018), and total RNAs were isolated. First-strand cDNAs were synthesized using the SuperScript III First-Strand synthesis kit (ThermoFisher Scientific, 18080-051) (see Supplementary Materials and Methods).

Single-nucleus RNA sequencing (snRNA-Seq)

Nuclei isolation and single-nucleus RNA sequencing were performed by the Singulomics Corporation (Singulomics.com, Bronx, NY, USA) (see Supplementary Materials and Methods).

Spatial Transcriptomics

The samples were sectioned and placed on a pre-chilled Visium Spatial Gene Expression Slide (10x Genomics, PN-2000233). The tissue sections were processed following 10x Genomics protocols (PN-1000187, PN-1000215) (see Supplementary Materials and Methods).

Measurement of hepatic TG and plasma insulin levels

Liver samples were harvested from mice with or without liver-innervating sensory neurons. Tissue samples were weighed and homogenized in 1 mL of a diluted NP-40 solution to solubilize triglycerides (see Supplementary Materials and Methods).

For measure plasma insulin levels, blood samples from the experimental and control groups were collected from the retroorbital plexus using heparinized capillary tubes (see Supplementary Materials and Methods).

Animal behavior tests

For the open field exploration test, mice were placed in the center of a chamber measured 40 cm (length) x 40 cm (width) x 40 cm (height) and allowed to explore the chamber for 10 min freely. To perform the elevated plus maze test, mice were placed in the central area of the maze consisting of four arms in the shape of a plus sign elevated approximately 1 m from the ground. Mice were allowed to explore the maze for 5 min freely. To perform the light-dark box test, mice were placed in the box that consists of two chambers, one light and one dark. Detailed methods were described in Supplementary Materials and Methods.

Statistics

All statistical results are presented as the mean ± SEM. Statistical analyses were performed using GraphPad Prism, version 10.0. Two-tailed *t*-tests were used to calculate the p-values for pair-wise comparisons. Time-course comparisons between groups were analyzed using a two-way repeated-measures analysis of variance (RM ANOVA) with Sidak's correction for multiple comparisons. Data were considered significantly different when the probability value was less than 0.05.

Results

Molecular identification of vagal sensory neurons innervating the liver

To determine whether the vagal sensory neurons innervate the liver, we expressed the Cre recombinase in the vagus nerve ganglia by administering retrograde adeno-associated viruses (AAVrg) encoding the Cre gene (AAVrg-Cre) to the liver of Rosa26-eGFP^{f} mice (Fig. 1a). Under these conditions, AAVrg-Cre viruses were taken up by the peripheral vagus nerve terminals and transported toward the cell body. GFP immunostaining revealed the presence of GFP-positive cells in the nodose ganglion (Fig. 1b). Contrary to previous studies showing that vagal sensory neurons innervating the liver are primarily located in the left nodose ganglion in rats[111, 17], the number of GFP-positive neurons was similar in both vagus nerve ganglia (Fig. 1c).

We then sought to determine the molecular identity of liver-innervating vagal sensory neurons by performing snRNA-Seq of vagal sensory neurons in Rosa26-eGFP^{f} mice injected with AAVrg-Cre into the liver (Fig. 1d). We identified approximately 9,000 cells from 30 nodose ganglia collected from 8 males and 7 females. Among them, approximately 6,000 cells had neuronal marker genes such as *Map2*, *Syn1*, *Syn2*, and *Slc17a6*. However, we found only 7

genetically tagged vagal sensory neurons (Supplementary Table 1) because of the technical limitations associated with a limited number of liver-innervating vagal sensory neurons. We grouped the seven vagal sensory neurons innervating the liver and compared them with other vagal sensory neurons. They expressed neuronal marker genes such as *Syn1*, *Scn10a*, *Kcnc2*, and *Avil*[18]. These sensory neurons expressed several ion channel subtypes including *Trpv1*, *Trpm3*, *Trpa1*, and *Piezo2* (Fig. 1f), indicating that they are polymodal sensory neurons. These neurons also expressed *Oprm1*, *Npy2R*, *Cckar*, and *Cnr1*. Intriguingly, liver-innervating vagal sensory neurons also highly expressed genes involved in lipid metabolism such as *Acyl*, *Fasn*, and *Scd2*, compared to other vagal sensory neurons (Fig. 1g). Additionally, these neurons expressed genes related to cell adhesion, neuronal migration, axonal growth, and survival. These genes included *Unc5c*, *Nrg1 and 3*, *Tmeff2*, *Kirrel3*, and others (Fig. 1h). Hence, our results suggest that liver-innervating vagal sensory neurons are polymodal and are molecularly distinct from other vagal sensory neurons.

The liver is innervated by a subset of Avil-positive vagal sensory neurons

Based on our snRNA-Seq results and a previous study indicating that chemosensitive vagal sensory neurons express *Avil* gene[10], we used the Avil^{CreERT2} strain to identify vagal sensory neurons that innervate the liver. Additionally, we employed AAVrg-FLEX-jGCamp7s, which expresses Cre-inducible jGCamp7s, due to the observation that GFP expression with this vector was more robust compared to other AAV vectors encoding eGFP and tdTomato. Administering AAVrg-FLEX-jGCamp7s to the medial and left lobes of the livers of Avil^{CreERT2} mice resulted in the selective labeling of liver-innervating vagal sensory neurons (Fig. 1i, j, and k). Both nodose ganglia exhibited a small number of GFP-positive cells. Approximately 10% of Avil-positive vagal sensory neurons were positive for GFP.

To investigate their peripheral nerve terminals, we crossbred the Avil^{CreERT2} strain with floxed-Stop channelrhodopsin (ChR2)-tdTomato mice (Avil$^{CreERT2:ChR2\text{-}tdTomato}$), as the ChR2-tdTomato fusion protein displayed strong expression in nerve terminals (Fig. 2a). Immunostaining revealed numerous tdTomato-positive nerve fibers in the periportal area (Fig. 2b), indicating that they were the nerve fibers originated in Avil-positive sensory neurons. Next, we administered anterograde AAV1-FLEX-GFPsm-Myc directly into the left nodose ganglion of Avil^{CreERT2} mice (Fig. 2c and d), expecting that the anterograde viruses were directed toward the

peripheral nerve terminals. We found the anterogradely-labeled GFP-and Myc-positive nerve terminals primarily around the periportal, but not pericentral, areas (Fig. 2d and Supplementary Fig. 1a and b). We further examined their peripheral nerve terminals by injecting retrograde AAV (AAVrg)-FLEX-jGCamp7s into the livers of Avil^{CreERT2} mice (Fig. 2e and Supplementary Fig. 1c). Avil-positive nerve terminals were co-labeled with an anti-GFP antibody in the periportal area (Fig. 2f), whereas there were no Avil-positive nerves in the pericentral zone (Suppl. Fig. 1d). Additionally, co-staining with an antibody against the presynaptic marker synapsin 1 (Syn1) revealed that GFP-positive nerve terminals were positive for Syn1, indicating that these are nerve terminals (Fig. 2g). Taken together, our tracing results strongly support that the liver receives synaptic input from Avil-positive vagal sensory neurons.

We then examined the central projection sites of the vagal sensory neurons innervating the liver in the medulla. We used brainstem tissues from Avil^{CreERT2} mice injected with AAVrg-FLEX-GFP into the liver (Supplementary Fig. 2a). Following the tissue-clearing process, we conducted a 3D imaging analysis of the tissues, which revealed GFP-positive puncta and nerve terminals in the NTS and the area postrema (AP) (Supplementary Fig. 2b and Supplementary Movie 1). Additionally, scattered GFP-positive puncta were observed in the dorsal motor nucleus of the vagus (DMV). (Supplementary Fig. 2b and Suppl. Movie 1).

Loss of liver-innervating vagal sensory neurons causes weight loss and increases energy expenditure.

The hepatic portal vein carries nutrients and hormones from the gastrointestinal tract[19]. As vagal sensory neurons sent projections to the periportal regions of the liver and expressed lipid-sensing TRP receptors (Fig. 1f), it is possible that vagal sensory neurons innervating the liver may detect changes in nutrients[20]. We thus investigated the impact of the loss of the liver-brain axis on energy balance under obesogenic conditions. To ablate liver-innervating vagal sensory neurons, we expressed genetically engineered taCaspase-3 (taCasp3)[21] in the vagal sensory neurons innervating the liver by injecting AAVrg-FLEX-taCasp3-TEVp into the livers of Avil^{CreERT2} mice (Fig. 3a). To determine whether the retrograde expression of taCasp3-TEVp ablates liver-projecting vagal sensory neurons, we administered the retrograde tracer Fluoro-Gold into livers of Avil^{CreERT2} mice injected with AAVrg-FLEX-taCasp3-TEVp and examined the number of Fluoro-Gold-positive vagal sensory neurons (Supplementary Fig. 3a). There was a

significant reduction of liver-projecting vagal sensory neurons (Supplementary Fig. 3b, c, and d). Moreover, unlike the Avil^{CreERT2} mice injected with AAVrg-FLEX-jGCamp7s, we did not observe any GFP-positive nerve terminals in the periportal areas of AAVrg-FLEX-taCasp3-TEVp injected mice (Supplementary Fig. 3e, f, and g), which provides further evidence of the loss of liver-projecting vagal sensory innervation of the liver.

Under these experimental conditions, measurements of body weight showed a significant difference in body weight between the groups. The experimental male mice gained significantly less weight than control mice (Fig. 3b). This was accompanied by a significant decrease in both fat mass and fat-free mass in the experimental mice compared with the controls (Fig. 3c and d). We then examined whether changes in food intake and/or energy expenditure in male mice fed HFD result in decreased body weight. Both groups consumed similar amounts of food during the light and dark phases (Fig. 3e). We thus investigated if there was a difference in the energy expenditure between the groups. The experimental mice consumed more O_2 and produced more CO_2 than the control mice (Fig. 3f and g), resulting in a significant increase in total energy expenditure (TEE) over a 24-hour period (Fig. 3h). The respiratory energy ratio (RER) and locomotor activity did not differ between the groups (Fig. 3i, j, and k). Analysis of covariance (ANCOVA) using body weight as a covariate showed no differences in the slopes (Fig. 3l), suggesting that body fat did not have a substantial impact on TEE.

Ablating liver-innervating vagal sensory neurons caused a reduction in body weight in female mice as well (Fig. 3m). This reduction was primarily associated with decreased fat mass but not fat-free mass (Fig. 3n and o). Like males, female mice lacking hepatic vagal sensory neurons displayed no difference in food intake compared to controls (Fig. 3p). Indirect calorimetry analysis revealed that VO_2, VCO_2, and TEE in experimental mice were significantly higher than those in control mice (Fig. 3q, r, and s). There were no differences in the RER and locomotor activity between the two groups (Fig. 3t, u, and v). Intriguingly, ANCOVA analysis revealed that body weight significantly influenced TEE (Fig. 3w), suggesting that fat tissue may significantly impact energy expenditure in females.

Loss of liver-innervating vagal sensory neurons improves glucose tolerance in mice fed HFD

We next examined the impact of the loss of the liver-brain axis on glucose homeostasis during HFD feeding. Measuring the glucose levels following 10 weeks of HFD feeding revealed that both non-fasting and fasting blood glucose levels were significantly lower in the experimental male mice than in the control male mice (Supplementary Fig. 4a and b). Intraperitoneal glucose tolerance tests (i.p.GTT) showed that the blood glucose levels of the experimental mice in response to a bolus of glucose (i.p., 2 g/kg) were significantly lower than those of the control mice (Supplementary Fig. 4c and d). Insulin tolerance tests (ITT 1 U /kg, i.p.) revealed improved tolerance in experimental males compared to control mice (Supplementary Fig. 4e). This improved insulin tolerance in the experimental group was associated with decreased basal and fasting insulin levels relative to those in the control group (Supplementary Fig. 4f and g).

Likewise, female mice lacking hepatic vagal sensory neurons exhibited lower basal and fasting blood glucose levels than the control females (Supplementary Fig. 4h and i). Female mice in the experimental group displayed improved glucose tolerance during the GTT compared to the control group (Supplementary Fig. 4j and k). However, there was no noticeable difference in insulin sensitivity between the two groups during the ITT (Supplementary Fig. 4l). The basal insulin levels were significantly lower in the experimental group compared to the control group, while the fasting insulin levels were similar (Suppl. Fig. 4m and n).

Loss of liver-innervating vagal sensory neurons prevents hepatic steatosis in HFD-fed mice.

We investigated whether the loss of the liver-brain axis affects hepatic lipid metabolism. The livers of the control group turned yellowish, while the livers of the experimental mice remained red (Fig. 4a). The liver weight was significantly lower in the experimental mice than in the control mice (Fig. 4b). Hematoxylin and Eosin (H&E) staining revealed clear differences between the groups (Fig. 4c). Specifically, mice displayed numerous large and small lipid droplets, primarily in the pericentral regions, compared to experimental mice. Oil Red O staining further confirmed hepatic fat accumulation in control mice (Fig. 4d).

Given the lack of lipid droplets in the livers of experimental male mice, we measured hepatic triglyceride (TG) levels. The experimental mice displayed a substantial decrease in hepatic TG levels compared with the control mice (Fig. 4e). RT-qPCR analysis of liver tissues from the experimental mice revealed a significant decrease in the expression of the lipogenic

transcription factor *Srebp-1c*, in comparison to the controls (Fig. 4f). This was accompanied by downregulation of its target genes, including *Acaca*, *Fasn*, and *Scd1* (Fig. 4f). In addition, the impairment of the liver-brain axis downregulated the fatty acid translocase *Cd36* and the fatty acid transmembrane transporters *Fatp3* and *Fatp4* gene expression (Fig. 4g). These results indicate that the loss of the liver-brain axis may lead to a reduction in *de novo* lipogenesis (DNL) and fatty acid uptake, thereby preventing the onset of hepatic steatosis in male mice fed HFD.

In female mice, there was no visible difference in liver color (Fig. 4h). The liver weight was slightly but significantly reduced in the experimental group compared to the control group (Fig. 4i). H & E and Oil red O staining revealed that the control group exhibited small lipid droplets in the liver parenchyma, whereas the experimental group displayed fewer such droplets (Fig. 4j and k). The experimental mice demonstrated a decrease in hepatic TG compared to the control mice (Fig. 4l). In contrast to the experimental male mice, the experimental female mice showed no significant difference in the expression of the lipogenic genes (Fig. 4m). Nonetheless, female mice lacking liver-innervating vagal sensory neurons exhibited decreased *Cd36* and *Fatp3* expression levels (Fig. 4n). Taken together, these novel findings support the interpretation that liver-innervating vagal sensory neurons are crucial for the emergence of hepatic steatosis in mice during the development of obesity.

The male control mice displayed dense lipid accumulation in the pericentral areas compared to the experimental mice. We conducted further analysis to determine if there are distinct gene expression patterns throughout the hepatic zonation in both groups by performing spatial transcriptomics (Fig. 5). Pericentral, midlobular, and periportal clusters were identified based on known zonation markers (Fig, 5a). We found that approximately 500 genes in the PC and PP areas were significantly different between the groups (Fig. 5b and Supplementary Table 2 and 3) and that the midlobular areas exhibited about 300 differentially expressed genes (DEGs) (Fig. 5b and Supplementary Table 4). Among these genes, the loss of liver-projecting vagal sensory neurons resulted in the opposite regulation of two transcription factors, specifically *Irf6* and *Tbx3* (Fig. 5c). It has been described that HFD feeding downregulated *Irf6* expression in hepatocytes and that overexpression of *Irf6* in hepatocytes reduced hepatic steatosis[22]. In contrast, deletion of *Tbx3* improved hepatic steatosis in mice fed a high-fat diet[23]. The control mice exhibited an elevated expression of *Srebf1*, *Fasn*, *Scd1*, and *Cd36* genes (Fig. 5c), consistent with our qPCR results. In addition, NAFLD- and liver fibrosis-related genes such as *Sptlc2*[24],

Col3a1[25], *Vim*[26] were downregulated in mice without liver-projecting vagal sensory neurons. In contrast, the control mice exhibited a downregulation of *Slc2a1* and *Avpr1a* as described in individuals with NAFLD[27, 28].

We also conducted a selective gene ontology (GO) analysis of the DEGs in each zonation using Enrichr-KG[29], which identified the top 5 enriched GO terms in biological process (Fig. 5D). These included "cotranslational protein targeting to membrane" (GO:0006613), "SRP-dependent cotranslational protein targeting to membrane" (GO:0006614), "protein targeting to ER" (GO:0045047), "cytoplasmic translation" (GO:0002181), and "cellular protein metabolic process" (GO:0044267). According to the mammalian phenotype ontology analysis[30], each zonation shared 4 terms, including "abnormal lipid homeostasis" (MP:0002118), "abnormal liver physiology" (MP:0000609), and "hepatic steatosis" (MP:0002628). Notably, each zonation had a unique GO term, such as "increased liver weight" (MP:0002981) in the PP group, "abnormal hepatocyte morphology" (MP:0000607) in the Mid group, and "abnormal circulating amino acid level" (MP:0005311) in the PC group. Furthermore, the Jesensen diseases ontology analysis revealed a term for "fatty liver disease" (Fig. 5d). These results further support that liver-projecting vagal sensory neurons play an important role on developing hepatic steatosis in mice fed HFD.

Loss of the liver-brain axis improves anxiety-like behavior in mice fed HFD.

Individuals with NAFLD have been found to have an increased risk of developing psychiatric disorders, including anxiety and depression. We conducted an open field exploration test, which is an initial screening for anxiety-like behavior[31]. Our experimental mice displayed increased time spent in the inner area and decreased time spent in the outer area, as well as increased distance traveled in the inner area. We then performed an elevated plus maze test that examines the natural tendency of mice to explore novel environments by giving the choice of spending time in open, unprotected maze arms or enclosed, protected arms[32] (Fig. 6f). The control mice spent more time in the closed arm (Fig. 6g) and made fewer entries into the open arms than the experimental group (Fig. 6g). The experimental mice displayed increased distance traveled in the center area (Fig. 6h). The light-dark box test that assesses a change in willingness to explore the illuminated, unprotected area revealed that the experimental mice exhibited increased time spent in the light area compared to the control group (Fig. 6j, k, and l). Similarly,

the female experimental mice displayed increased locomotor activity, increased time spent and distance in the inner area (Supplementary Fig. 5). All the results support the interpretation that mice without liver-projecting vagal sensory neurons exhibited improved anxiety-like behavior.

Discussion

Our single-nucleus RNA-seq analysis revealed that liver-projecting vagal sensory neurons were polymodal C-fiber sensory neurons described in the study by the Ernfors research group (i.e., NG12 to NG18[10]). In fact, polymodal C-fiber vagal sensory neurons expressed *Scn10a*, *Trpv1*, *Trpa1*, *Npy2r*, and *Cckar*[10] which were also expressed in liver-projecting vagal sensory neurons. Liver-innervating vagal sensory neurons were found mainly in the periportal area surrounding the hepatic arteries, bile ducts, and portal veins and expressed mechano-sensing Piezo channels[33], lipid-sensing TRPA1, TRPM3, and TRPV1 channels[34], and gut-derived hormone CCK receptors. This multimodality of liver-innervating vagal sensory neurons would be particularly important because hepatic homeostasis highly relies on adequate perfusion and microcirculation via the dual hepatic arterial and portal venous blood supply, as well as the fenestrated sinusoids. These anatomical and molecular features would enable them to accurately measure blood pressure, assess the levels of various nutrients and peptides, and relay this information to the brain for processing and interpretation.

Intriguingly, our study revealed a significant expression of genes associated with lipid metabolism in liver-projecting vagal sensory neurons, such as *Acly*, *Fasn*, and *Scd2*. It has been shown that fatty acid metabolism in the brain, particularly the hypothalamus, exerts a significant influence on the regulation of food intake and energy metabolism[35-37], suggesting that fatty acid metabolism and its associated metabolites in hypothalamic neurons may serve as indicators of nutrient status. Similarly, the increased lipogenic machinery in liver-innervating vagal sensory neurons may imply that they also possess the capability to control energy balance in response to changes in nutrient availability. Additionally, lipogenesis in neurons is critical for several aspects of neuronal function, including dendrite morphogenesis[38], axon growth and regeneration[39]. The UNC5 family of netrin receptors (UNC5C and 5D) is involved in axon guidance and mediates axon repulsion of neuronal growth cones in the developing nervous system[40]. Of particular interest is that netrin-1 was found to stimulate the regeneration of the hepatic vagal nerve and the proliferation of hepatocytes in mice following hepatectomy[41]. Thus, our initial findings from single-nucleus RNA sequencing provides significant information regarding their potential implications for a range of physiological processes.

The periportal region had dense innervation of vagal sensory neurons innervating the liver. As the portal vein delivers nutrients and hormones from the gut, liver-projecting vagal

sensory neurons could transmit this information to the NTS. Both local interneurons and projection neurons in the NTS were implicated in the control of various body functions. For instance, local GABAergic interneurons influenced the activity of liver-projecting parasympathetic cholinergic neurons in the DMV, thereby regulating the hepatic glucose output[42]. Norepinephrine-expressing neurons in the NTS controlled feeding behavior[43-45]. Interestingly, activation of the NE-expressing neurons in the NTS (NTS^{NE}) to CGRP-expressing neurons in the PBN pathway reduced[44], whereas stimulation of the NTS^{NE} to agouti-related peptide (Agrp)-containing neurons in the arcuate nucleus of the hypothalamus pathway promoted, feeding[43]. The anti-obesity effect that we observed would be due to the fact that the brain receives the inadequate information on excess energy balance via vagal sensory neurons innervating the liver. Consequently, this sensory impairment would cause an increase in energy expenditure instead of storing excess nutrients in the liver.

The decrease in hepatic steatosis in our preparations is likely attributable to the decrease in DNL. In fact, the experimental mice exhibited a decrease in *Srebf1* and its target genes. The significant reduction in *Cd36* expression was also observed in the livers of experimental mice. This decrease may have a significant impact on DNL since CD36 is involved not only in transporting fatty acids but also in SREBP1 processing in the liver[46]. Interestingly, HFD feeding appeared to have an opposite effect on *Irf6* and *Tbx3* expression in the PC of control mice compared to the experimental mice. *Irf6* overexpression in hepatocytes reduced hepatic steatosis[22], while hepatic *Tbx3* deletion improved hepatic steatosis in mice fed a HFD[23]. These three transcription factors and *Cd36* could be crucial downstream targets of liver-projecting vagal sensory input. The enrichment analysis showed that each zonation possessed a unique GO term, including "increased liver weight" in the PP group, "abnormal hepatocyte morphology" in the Mid group, and "abnormal circulating amino acid levels" in the PC group. This suggests that each zonation may have distinct impacts on the liver, leading to different types of abnormalities.

The animal behavior tests we conducted showed that the experimental mice were more inclined to explore novel and unprotected areas, suggesting that they were less anxious and more motivated than the control mice. Although it appears that impaired hepatic lipid metabolism significantly affects psychiatric disorders[13-15], the underlying mechanisms remains poorly understood. Our results suggests that liver-innervating vagal sensory neurons may play an important role in developing psychiatric disorders in patients with obesity and NAFLD. An

implantable vagus nerve stimulator has been approved by the Food and Drug Administration to treat epilepsy and depression. Modulating the liver-brain axis via the vagus nerve may offer a promising therapeutic approach for improving lipid metabolism, glucose homeostasis, and affective disorders in obesity and diabetes.

References:

1. Waise TMZ, Dranse HJ, Lam TKT. The metabolic role of vagal afferent innervation. Nat Rev Gastroenterol Hepatol 2018;15:625-636.
2. Bassi JK, Connelly AA, Butler AG, et al. Analysis of the distribution of vagal afferent projections from different peripheral organs to the nucleus of the solitary tract in rats. J Comp Neurol 2022;530:3072-3103.
3. Bai L, Mesgarzadeh S, Ramesh KS, et al. Genetic Identification of Vagal Sensory Neurons That Control Feeding. Cell 2019;179:1129-1143 e23.
4. Chang RB, Strochlic DE, Williams EK, et al. Vagal Sensory Neuron Subtypes that Differentially Control Breathing. Cell 2015;161:622-633.
5. Makhmutova M, Weitz J, Tamayo A, et al. Pancreatic beta-Cells Communicate With Vagal Sensory Neurons. Gastroenterology 2021;160:875-888 e11.
6. Williams EK, Chang RB, Strochlic DE, et al. Sensory Neurons that Detect Stretch and Nutrients in the Digestive System. Cell 2016;166:209-21.
7. Zhao Q, Yu CD, Wang R, et al. A multidimensional coding architecture of the vagal interoceptive system. Nature 2022;603:878-884.
8. Han W, Tellez LA, Perkins MH, et al. A Neural Circuit for Gut-Induced Reward. Cell 2018;175:665-678 e23.
9. Borgmann D, Ciglieri E, Biglari N, et al. Gut-brain communication by distinct sensory neurons differently controls feeding and glucose metabolism. Cell Metab 2021;33:1466-1482 e7.
10. Kupari J, Haring M, Agirre E, et al. An Atlas of Vagal Sensory Neurons and Their Molecular Specialization. Cell Rep 2019;27:2508-2523 e4.
11. Carobi C, Magni F. The afferent innervation of the liver: a horseradish peroxidase study in the rat. Neurosci Lett 1981;23:269-74.
12. Berthoud HR, Kressel M, Neuhuber WL. An anterograde tracing study of the vagal innervation of rat liver, portal vein and biliary system. Anat Embryol (Berl) 1992;186:431-42.
13. Gangopadhyay A, Ibrahim R, Theberge K, et al. Non-alcoholic fatty liver disease (NAFLD) and mental illness: Mechanisms linking mood, metabolism and medicines. Front Neurosci 2022;16:1042442.
14. Shang Y, Widman L, Hagstrom H. Nonalcoholic Fatty Liver Disease and Risk of Dementia: A Population-Based Cohort Study. Neurology 2022;99:e574-e582.
15. Soto-Angona O, Anmella G, Valdes-Florido MJ, et al. Non-alcoholic fatty liver disease (NAFLD) as a neglected metabolic companion of psychiatric disorders: common pathways and future approaches. BMC Med 2020;18:261.
16. Matsumoto K, Mitani TT, Horiguchi SA, et al. Advanced CUBIC tissue clearing for whole-organ cell profiling. Nat Protoc 2019;14:3506-3537.
17. Teratani T, Mikami Y, Nakamoto N, et al. The liver-brain-gut neural arc maintains the T(reg) cell niche in the gut. Nature 2020;585:591-596.
18. Hasegawa H, Abbott S, Han BX, et al. Analyzing somatosensory axon projections with the sensory neuron-specific Advillin gene. J Neurosci 2007;27:14404-14.
19. Bacharach SZ, Tordoff MG, Alhadeff AL. Glucose Sensing in the Hepatic Portal Vein and Its Role in Food Intake and Reward. Cell Mol Gastroenterol Hepatol 2023;16:189-199.

20. Niijima A, Torii K, Uneyama H. Role played by vagal chemical sensors in the hepato-portal region and duodeno-intestinal canal: an electrophysiological study. Chem Senses 2005;30 Suppl 1:i178-9.
21. Yang CF, Chiang MC, Gray DC, et al. Sexually dimorphic neurons in the ventromedial hypothalamus govern mating in both sexes and aggression in males. Cell 2013;153:896-909.
22. Tong J, Han CJ, Zhang JZ, et al. Hepatic Interferon Regulatory Factor 6 Alleviates Liver Steatosis and Metabolic Disorder by Transcriptionally Suppressing Peroxisome Proliferator-Activated Receptor gamma in Mice. Hepatology 2019;69:2471-2488.
23. Wang Z, Zhu S, Jia Y, et al. Positive selection of somatically mutated clones identifies adaptive pathways in metabolic liver disease. Cell 2023;186:1968-1984.e20.
24. Mardinoglu A, Agren R, Kampf C, et al. Genome-scale metabolic modelling of hepatocytes reveals serine deficiency in patients with non-alcoholic fatty liver disease. Nature Communications 2014;5.
25. Kostrzewski T, Snow S, Battle AL, et al. Modelling human liver fibrosis in the context of non-alcoholic steatohepatitis using a microphysiological system. Communications Biology 2021;4.
26. Wang WM, Zhang WS, Yang ZG. Vimentin (VIM) predicts advanced liver fibrosis in chronic hepatitis B patients: A random forest-derived analysis. Eur Rev Med Pharmacol Sci 2022;26:5164-5177.
27. Arendt BM, Comelli EM, Ma DWL, et al. Altered hepatic gene expression in nonalcoholic fatty liver disease is associated with lower hepatic n□3 and n□6 polyunsaturated fatty acids. Hepatology 2015;61:1565-1578.
28. Vazquez-Chantada M, Gonzalez-Lahera A, Martinez-Arranz I, et al. *Solute carrier family 2 member 1*is involved in the development of nonalcoholic fatty liver disease. Hepatology 2013;57:505-514.
29. Evangelista JE, Xie Z, Marino GB, et al. Enrichr-KG: bridging enrichment analysis across multiple libraries. Nucleic Acids Res 2023;51:W168-W179.
30. Smith CL, Goldsmith CA, Eppig JT. The Mammalian Phenotype Ontology as a tool for annotating, analyzing and comparing phenotypic information. Genome Biol 2005;6:R7.
31. Sestakova N, Puzserova A, Kluknavsky M, et al. Determination of motor activity and anxiety-related behaviour in rodents: methodological aspects and role of nitric oxide. Interdiscip Toxicol 2013;6:126-35.
32. Bailey KR, Crawley JN. Anxiety-Related Behaviors in Mice. In: nd, Buccafusco JJ, eds. Methods of Behavior Analysis in Neuroscience. Boca Raton (FL), 2009.
33. Zeng WZ, Marshall KL, Min S, et al. PIEZOs mediate neuronal sensing of blood pressure and the baroreceptor reflex. Science 2018;362:464-467.
34. Ciardo MG, Ferrer-Montiel A. Lipids as central modulators of sensory TRP channels. Biochim Biophys Acta Biomembr 2017;1859:1615-1628.
35. de Moura RF, Nascimento LF, Ignacio-Souza LM, et al. Hypothalamic stearoyl-CoA desaturase-2 (SCD2) controls whole-body energy expenditure. Int J Obes (Lond) 2016;40:471-8.
36. Gao S, Moran TH, Lopaschuk GD, et al. Hypothalamic malonyl-CoA and the control of food intake. Physiol Behav 2013;122:17-24.
37. Kim EK, Miller I, Aja S, et al. C75, a fatty acid synthase inhibitor, reduces food intake via hypothalamic AMP-activated protein kinase. J Biol Chem 2004;279:19970-6.

38. Ziegler AB, Thiele C, Tenedini F, et al. Cell-Autonomous Control of Neuronal Dendrite Expansion via the Fatty Acid Synthesis Regulator SREBP. Cell Rep 2017;21:3346-3353.
39. Ewan EE, Avraham O, Carlin D, et al. Ascending dorsal column sensory neurons respond to spinal cord injury and downregulate genes related to lipid metabolism. Sci Rep 2021;11:374.
40. Yamagishi S, Bando Y, Sato K. Involvement of Netrins and Their Receptors in Neuronal Migration in the Cerebral Cortex. Front Cell Dev Biol 2020;8:590009.
41. Wang Z, Jiang T, Aji T, et al. Netrin-1 promotes liver regeneration possibly by facilitating vagal nerve repair after partial hepatectomy in mice. Cell Signal 2022;91:110227.
42. Boychuk CR, Smith KC, Peterson LE, et al. A hindbrain inhibitory microcircuit mediates vagally-coordinated glucose regulation. Sci Rep 2019;9:2722.
43. Aklan I, Sayar Atasoy N, Yavuz Y, et al. NTS Catecholamine Neurons Mediate Hypoglycemic Hunger via Medial Hypothalamic Feeding Pathways. Cell Metab 2020;31:313-326 e5.
44. Roman CW, Derkach VA, Palmiter RD. Genetically and functionally defined NTS to PBN brain circuits mediating anorexia. Nat Commun 2016;7:11905.
45. Rinaman L. Hindbrain noradrenergic A2 neurons: diverse roles in autonomic, endocrine, cognitive, and behavioral functions. Am J Physiol Regul Integr Comp Physiol 2011;300:R222-35.
46. Zeng H, Qin H, Liao M, et al. CD36 promotes de novo lipogenesis in hepatocytes through INSIG2-dependent SREBP1 processing. Mol Metab 2022;57:101428.

Figure legends

Figure 1. Molecular identification of vagal sensory neurons innervating the liver

a. Schematic illustration of our experimental configurations. AAVrg-Cre viruses were injected into the medial and left lobes of the livers of Rosa26-eGFP^{f} mice.

b. Image from confocal microscopy showing GFP-positive cells in the right nodose ganglion of Rosa26-eGFP^{f} mice injected with AAVrg-Cre into the liver. Scale bar, 100 μm

c. Graph showing the number of GFP-positive cells per section in the left and right nodose ganglia.

d. Schematic illustration depicting our experimental process.

e, **f**, **g**, and **h**. Graphs showing enriched genes in liver-projecting vagal sensory neurons (LP VN) compared to other vagal sensory neurons (VN) (neuronal marker genes (e), membrane receptors and ion channels (f), lipogenic genes (g), and genes related to axon growth and maturation (h)).

i. AAVrg-FLEX-jGcamp7s viruses were injected into the livers of Avil^{CreERT2} mice.

j and k. Images showing co-expression of GFP and Avil in a subset of neurons in the left and right nodose ganglia of Avil^{CreERT2} mice injected with AAVrg-FLEX-jGcamp7s into the liver. Upper panel: scale bar, 100 μm. Bottom panel: higher magnification view of the yellow square area. Arrowheads represent the vagal sensory neurons that innervate the liver. Scale bar, 10 μm

Figure 2. Avil-positive vagal sensory neurons send axonal projections to the periportal area.

a and **b**. Schematic illustration of the experimental conditions. We used Avil$^{CreERT2;ChR2\text{-}tdTomato}$ mice. Images showing expression of tdTomato at nerve terminals in the periportal area (b). Left panel, scale bar, 20 μm. Right panel: higher magnification view of the white square area, scale bar, 10 μm

c and **d.** Anterograde monosynaptic AAV-FLEX-GFPsm-myc viruses were injected into the left nodose ganglion of of Avil^{CreERT2} mice. Most nerve terminals were positive for GFP and Myc, indicating that they were the nerve terminals of Avil-positive vagal sensory neurons innervating the liver. Scale bar, 20 μm. Bottom panel: higher magnification view of the white square area. Arrowheads represent co-expression of Myc and GFP. Bottom panel: scale bar, 10 μm

e. AAVrg-FLEX-jGcamp7s viruses were injected into the livers of Avil^{CreERT2} mice.

f and **g**. Images showing that GFP-positive nerve terminals were also stained with Avil (red, f) and the presynaptic marker Syn1 (red, g). Upper panel: scale bar, 20 μm, Bottom panel: scale bar, 10 μm

Figure 3. Loss of the liver-brain axis reduces body weight and increases energy expenditure in mice fed HFD.

a. Schematic representation of the experimental configurations. AAVrg-FLEX-eGFP and AAVrg-FLEX-taCasp3-TEVp viral vectors were injected into the livers of Avil^{CreERT2} mice.

b. Graph showing the changes in body weight of the control (n= 16 mice) and experimental groups (n= 15 mice) (two-way ANOVA, ***p<0.001)

c and d. Graphs showing the differences in fat mass and fat-free mass between the two groups (control, n= 16 mice; experimental, n=15 mice; unpaired *t*-test, ***p<0.001, *p<0.05).

e. Graphs showing no difference in food intake between the two groups (control, n= 6 mice; experimental mice, n=7 mice).

f and **g.** Graphs showing an increase in O_2 consumption and CO_2 production in the experimental group compared to the control group (control, n= 6 mice; experimental mice, n=7 mice; unpaired *t*-test, **p<0.01, ***p<0.001).

h. Graph showing that the experimental mice exhibited a significant increase in TEE compared with the control group (control, n= 6 mice; experimental mice, n=7 mice; unpaired *t*-test, **p<0.01).

i, j, and k. Graphs showing the RER and locomotor activity (control, n= 6 mice; experimental mice, n=7 mice).

l. ANCOVA analysis showing no difference between the two groups (control, n= 6 mice; experimental mice, n=7 mice).

m. Graph showing the changes in body weight of the control and experimental groups (control, n= 15 mice; experimental mice, n= 21 mice; Two-way ANOVA, ***p<0.001).

n and o. Graphs show that the experimental mice exhibited lower fat mass than the controls (control, n= 15 mice; experimental mice, n= 21 mice; unpaired *t*-test, ***p<0.001).

p. Graphs showing no difference in food intake between the two groups (control, n= 5 mice; experimental mice, n= 8 mice).

q and **r.** Summary graph showing an increase in O_2 consumption and CO_2 production in the

experimental group compared to the control group (control, n= 6 mice; experimental mice, n= 5 mice; unpaired *t*-test, *p<0.05, **p<0.01).

s. Graph showing that the experimental mice displayed a greater TEE than the control group (control, n= 6 mice; experimental mice, n= 5 mice; unpaired *t*-test, **p<0.01).

t, u, and v. Graphs showing no differences in RER or locomotor activity between the groups (control, n= 6 mice; experimental mice, n= 5 mice).

w. ANCOVA analysis showing a significant difference in the slope between the groups (control, n= 6 mice; experimental mice, n= 5 mice, *p<0.05).

Figure 4. Loss of the liver-brain axis prevents hepatic steatosis in mice fed HFD.

a. Representative images of liver tissues from the control and experimental mice.

b. Graphs showing liver mass between the groups (n= 14 vs. 18 mice, unpaired *t*-test, **p<0.01)

c and d. . H&E (c) and Oil Red O (d) staining of liver tissues from the control and experimental mice. Nuclear staining with hematoxylin (blue)Scale bar, 100 μm.

e. Graph showing hepatic TG levels between the groups (n= 7 mice vs. 7 mice, unpaired *t*-test, ***p<0.001).

f. Summary graphs showing changes in hepatic mRNA expression of enzymes involved in lipid metabolism between the groups (control, n= 7; experimental, n= 7, unpaired t-test, *p<0.05, **p<0.01, ***p<0.001).

g. Summary graphs showing changes in hepatic mRNA expression of fatty acid uptake transports between the groups (control, n= 6-8 mice; experimental, n= 7 mice, unpaired t-test, *p<0.05, **p<0.01).

h. Images of liver tissues from the control and experimental mice.

i. Graphs showing that the liver mass of the experimental mice (n=9) was lower when compared to that of the control group (n= 11 mice, unpaired *t*-test, *p<0.05).

j and k. H&E (j) and Oil Red O (k) staining of liver tissues from the control and experimental mice. Scale bar, 50 μm.

l. Graph showing hepatic TG levels between the groups (n= 6 mice vs. 7 mice, unpaired *t*-test, *p<0.05).

m. Summary graph showing alterations in hepatic lipogenic gene expression levels (control, n= 7; experimental mice, n= 8).

n. Summary graph showing changes in hepatic fatty acid uptake transport expression levels (control, n= 8; experimental mice, n= 8, unpaired t-test, *p<0.05, **p<0.01).

Figure 5. Differential gene expression in the livers of mice with and without liver-innervating vagal sensory neurons.

a. Violin plots depicting the differential expression of the liver zonation marker genes in the pericentral, midlobular, and periportal areas between the groups.

b. Volcano plots illustrate the differences in gene expression across the zonation of the livers between the groups.

c. Violin plots displaying the enriched genes across the zonation of the livers between the groups.

d. Plots displaying the top GO terms in biological process, mammalian phenotype, and Jensen diseases across the zonation of the livers between the groups.

Figure 6. Deleting liver-innervating vagal sensory neurons improves anxiety-like behavior.

a. Schematic representation of the experimental configurations.

b. Representative tracks (in red) in the open field box for control (n= 9 mice) and experimental (n= 9 mice) mice.

c, **d**, and **e**. Graphs showing the total distance traveled in the box (c), the time spent (d) and the distance traveled in inner and outer zones (e) between the groups (n= 9 mice vs. 9 mice, two-tailed t-test, *p<0.05, ***p<0.001)

f. Representative tracks (in red) for control (n= 5 mice) and experimental (n= 5 mice) mice on the elevated plus maze.

g and **h**. Graphs showing the cumulative duration spent in the center, open, and closed arms (g) and the distance travels in the center, open, and closed arms between the groups (n= 5 mice vs. 5 mice, two-tailed t-test, *p<0.05, **p<0.01)

i. Representative tracks (in red) for control (n= 6 mice) and experimental (n= 6 mice) mice in the light-dark box.

j, k, and l. Graphs showing the distance traveled in the light area (j), the time spent in the light and dark zones, and the number of zone transition (l) for control (n= 6 mice) and experimental (n= 6 mice) mice. Two-tailed t-test, *p<0.05

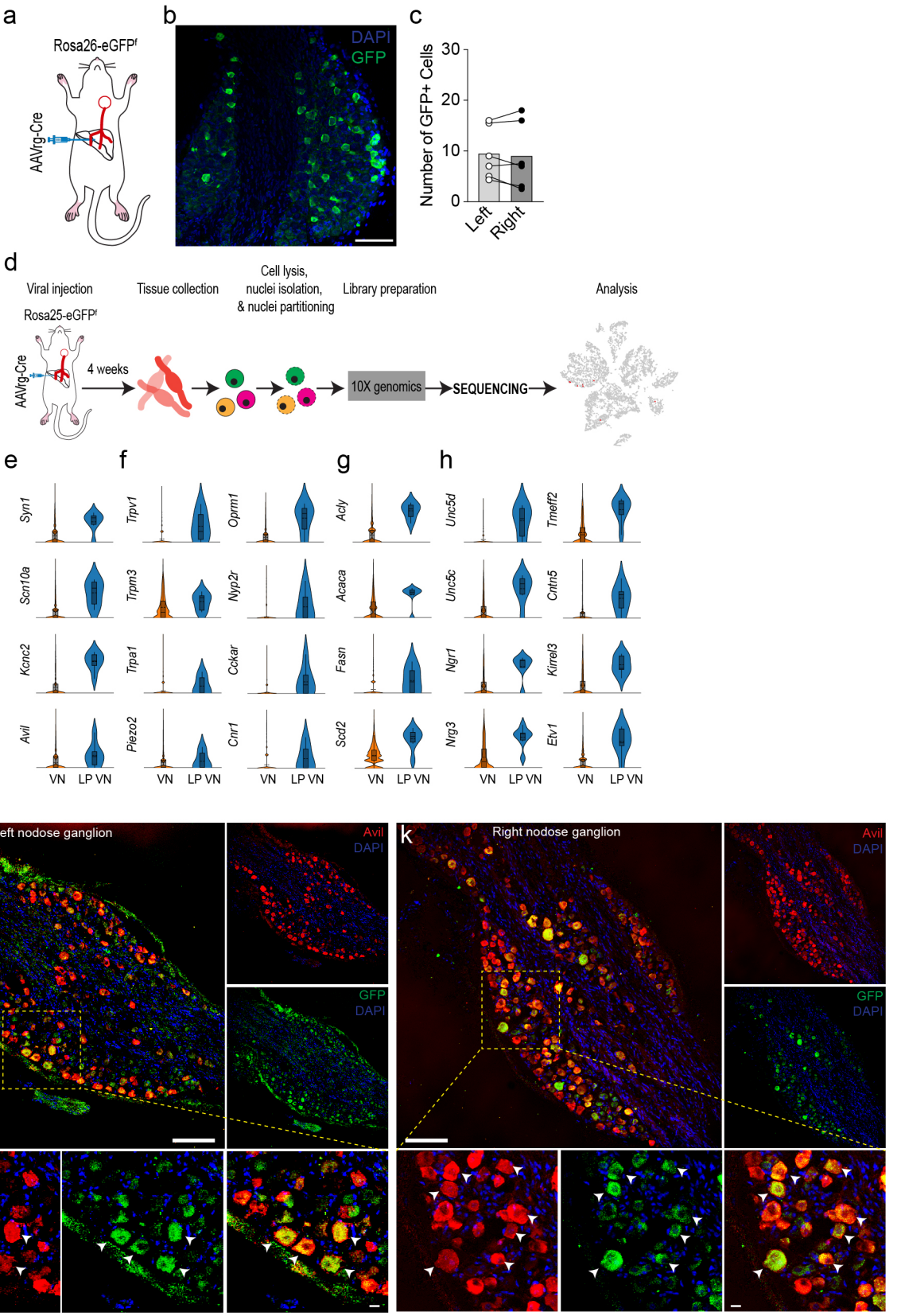
a
Rosa26-eGFPf
AAVrg-Cre
b
DAPI
GFP
c
Number of GFP+ Cells
30
20
10
0
Left
Right
d
Viral injection
Tissue collection
Cell lysis, nuclei isolation, & nuclei partitioning
Library preparation
Analysis
Rosa25-eGFPf
AAVrg-Cre
4 weeks
10X genomics
SEQUENCING
e
Syn1
Scn10a
Kcnc2
Avil
f
Trpv1
Trpm3
Trpa1
Piezo2
Oprm1
Nyp2r
Cckar
Cnr1
g
Acly
Acaca
Fasn
Scd2
h
Unc5d
Unc5c
Ngr1
Nrg3
Tmeff2
Cntn5
Kirrel3
Etv1
VN
LP VN
i
AvilCreERT2
AAVrg-FLEX-jGcamp7s
j
Left nodose ganglion
Avil
DAPI
GFP
DAPI
k
Right nodose ganglion
Avil
DAPI
GFP
DAPI

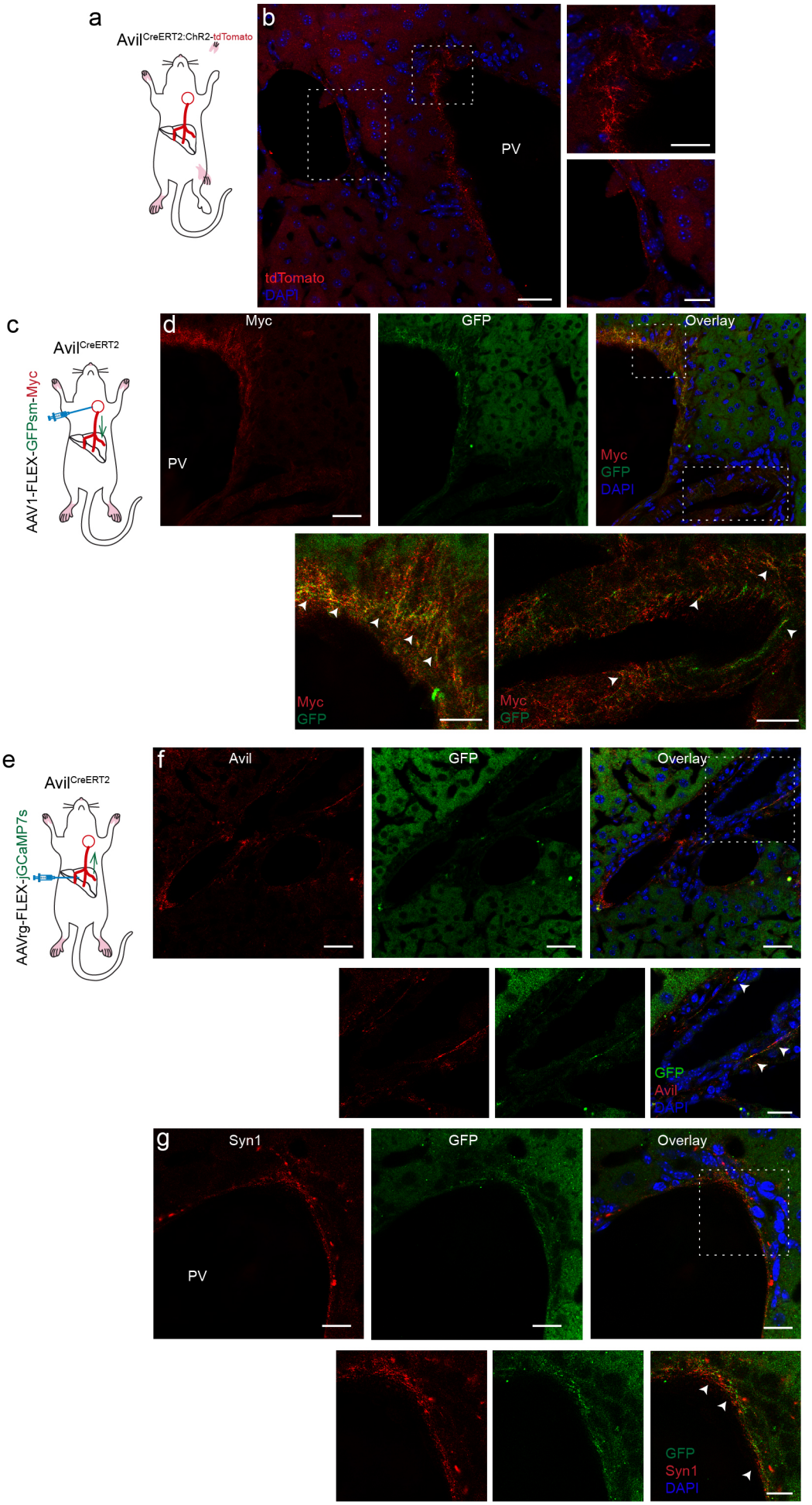
a
AvilCreERT2:ChR2-tdTomato
b
PV
tdTomato
DAPI
c
AvilCreERT2
AAV1-FLEX-GFPsm-Myc
d
Myc
GFP
Overlay
PV
Myc
GFP
DAPI
Myc
GFP
Myc
GFP
e
AvilCreERT2
AAVrg-FLEX-jGCaMP7s
f
Avil
GFP
Overlay
GFP
Avil
DAPI
g
Syn1
GFP
Overlay
PV
GFP
Syn1
DAPI

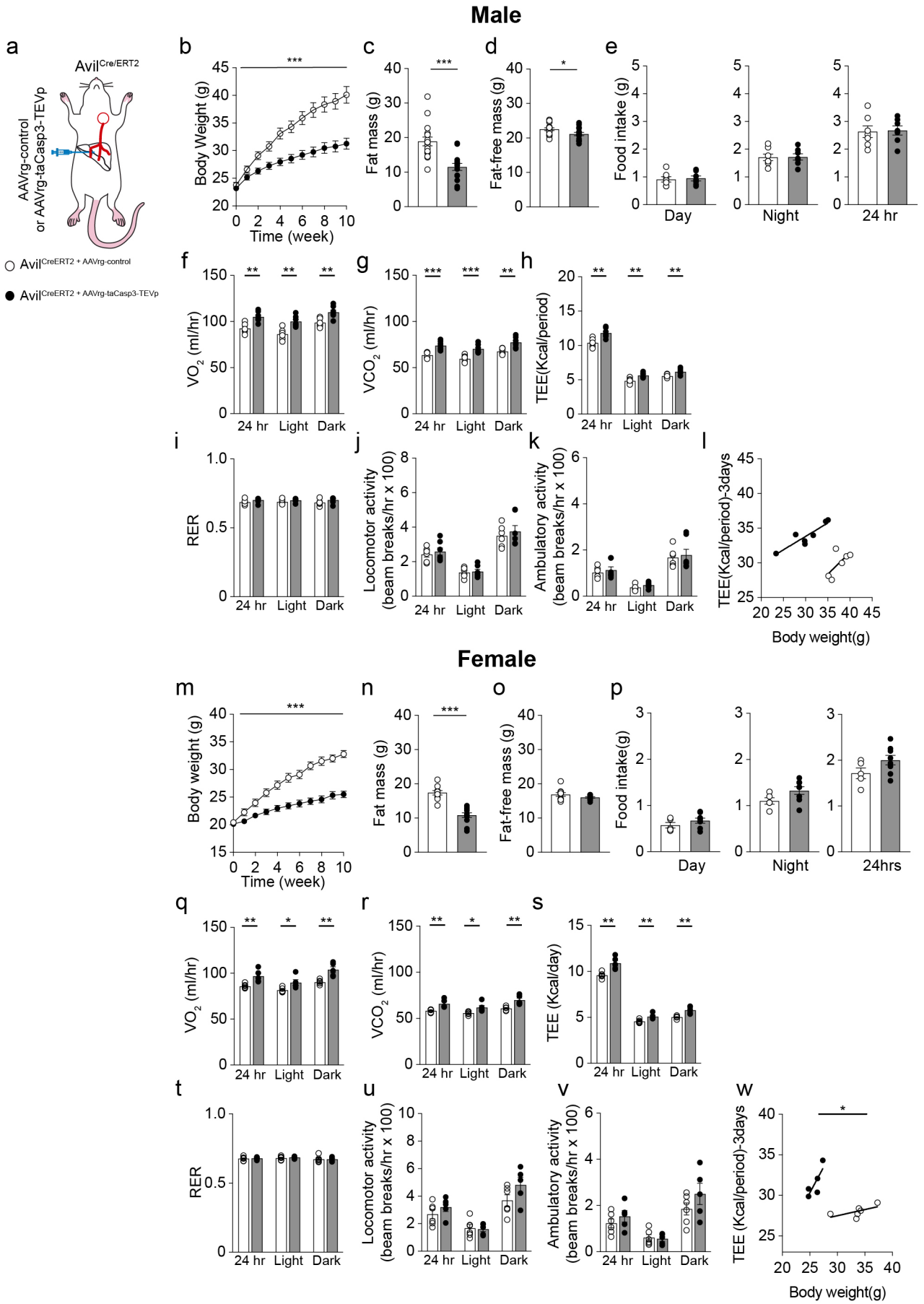
Male
a
Avil^Cre/ERT2
AAVrg-control
or AAVrg-taCasp3-TEVp
AvilCreERT2 + AAVrg-control
AvilCreERT2 + AAVrg-taCasp3-TEVp
b
Body Weight (g)
Time (week)
c
Fat mass (g)
d
Fat-free mass (g)
e
Food intake (g)
Day
Night
24 hr
f
VO2 (ml/hr)
g
VCO2 (ml/hr)
h
TEE(Kcal/period)
24 hr
Light
Dark
i
RER
j
Locomotor activity (beam breaks/hr x 100)
k
Ambulatory activity (beam breaks/hr x 100)
l
TEE(Kcal/period)-3days
Body weight(g)
Female
m
Body weight (g)
Time (week)
n
Fat mass (g)
o
Fat-free mass (g)
p
Food intake(g)
Day
Night
24hrs
q
VO2 (ml/hr)
r
VCO2 (ml/hr)
s
TEE (Kcal/day)
t
RER
u
Locomotor activity (beam breaks/hr x 100)
v
Ambulatory activity (beam breaks/hr x 100)
w
TEE (Kcal/period)-3days
Body weight(g)

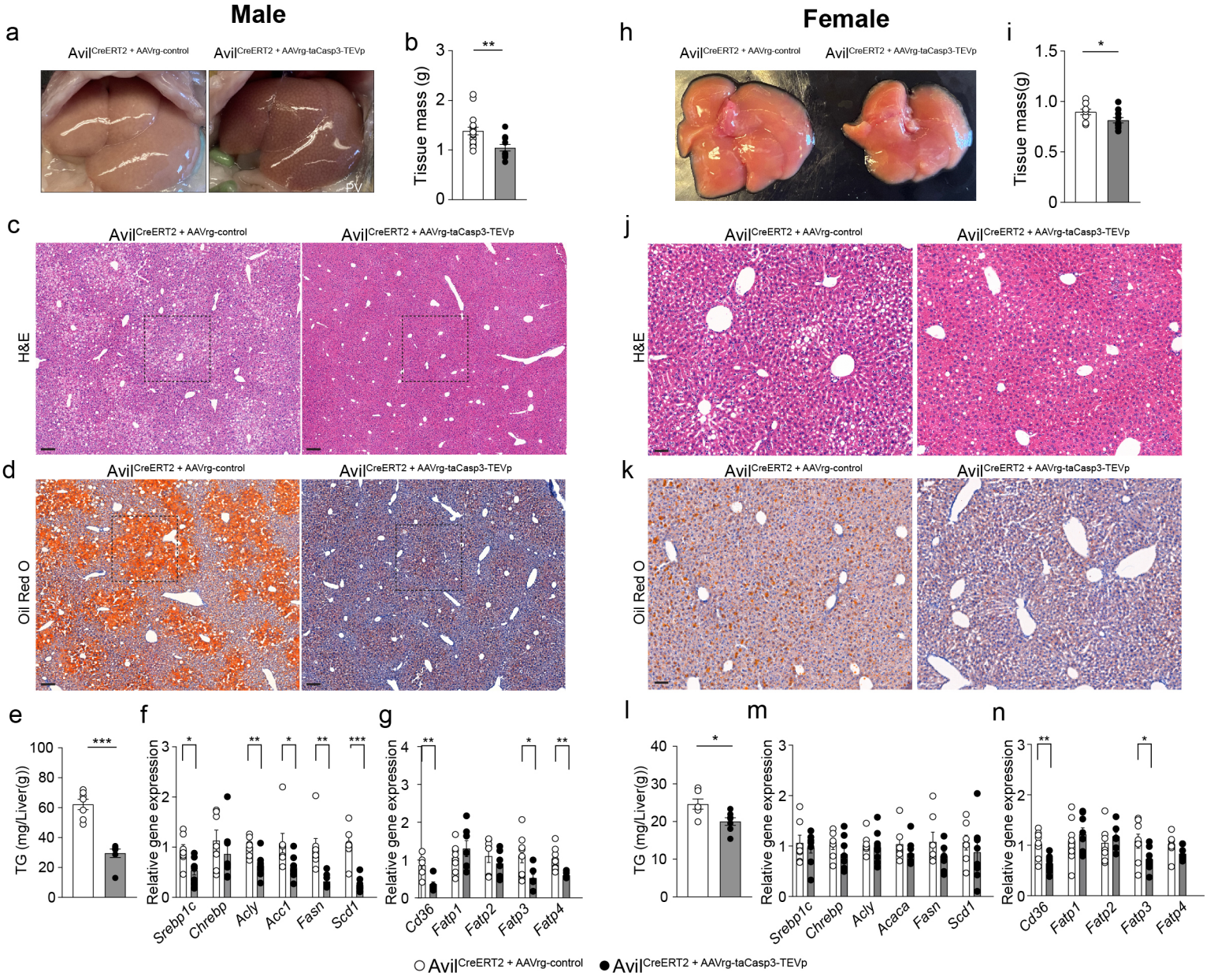
Male
Female
a
b
c
d
e
f
g
h
i
j
k
l
m
n
AvilCreERT2 + AAVrg-control
AvilCreERT2 + AAVrg-taCasp3-TEVp
PV
Tissue mass (g)
Tissue mass(g)
H&E
Oil Red O
TG (mg/Liver(g))
Relative gene expression
Srebp1c
Chrebp
Acly
Acc1
Fasn
Scd1
Acaca
Cd36
Fatp1
Fatp2
Fatp3
Fatp4

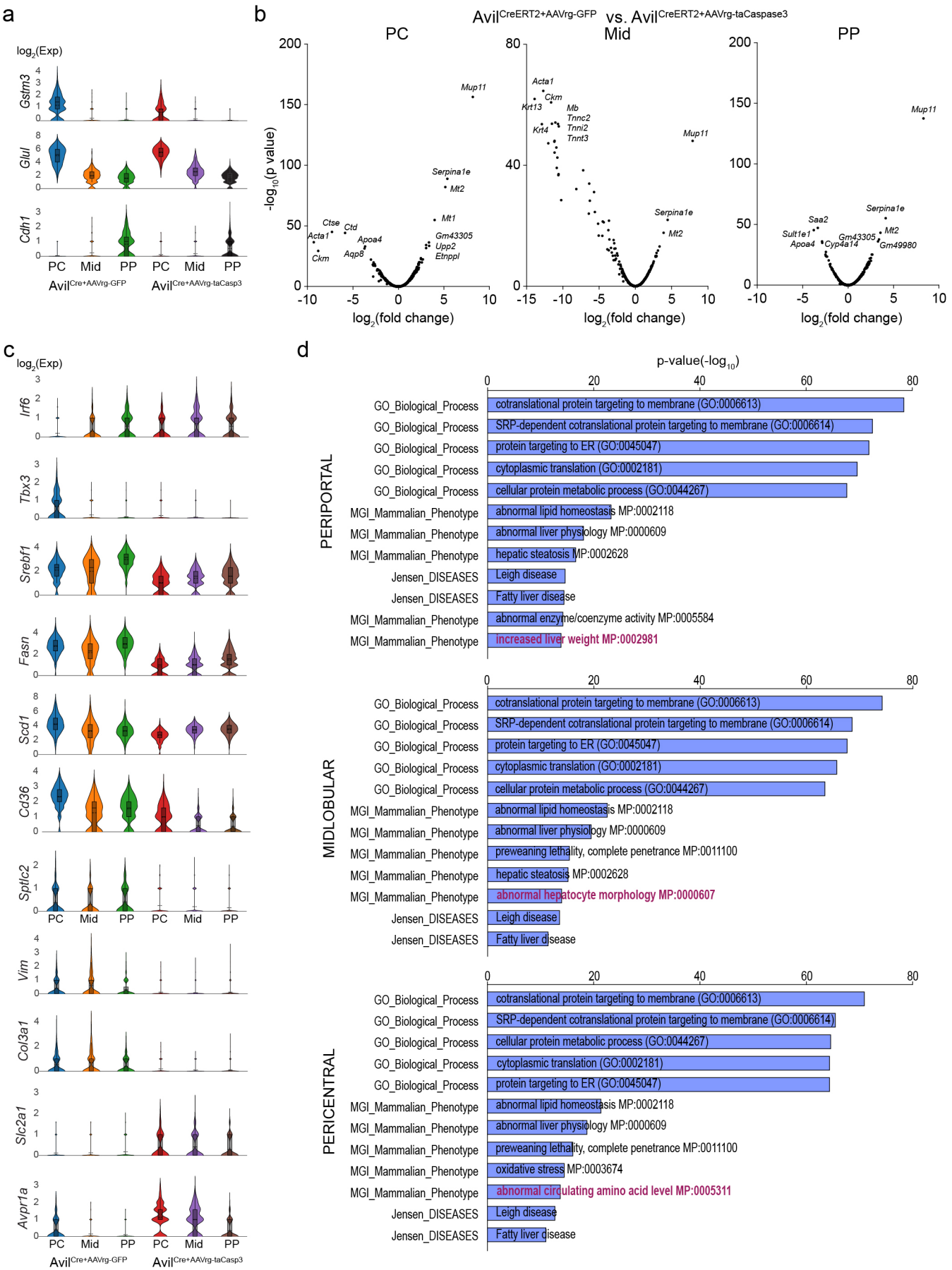
a
log2(Exp)
Gstm3
Glul
Cdh1
PC Mid PP PC Mid PP
AvilCre+AAVrg-GFP
AvilCre+AAVrg-taCasp3
b
AvilCreERT2+AAVrg-GFP vs. AvilCreERT2+AAVrg-taCaspase3
PC
Mid
PP
-log10(p value)
log2(fold change)
Mup11
Serpina1e
Mt2
Mt1
Gm43305
Upp2
Etnppl
Ctse
Ctd
Acta1
Ckm
Apoa4
Aqp8
Krt13
Krt4
Mb
Tnnc2
Tnni2
Tnnt3
Saa2
Sult1e1
Apoa4
Cyp4a14
Gm49980
c
log2(Exp)
Irf6
Tbx3
Srebf1
Fasn
Scd1
Cd36
Sptlc2
Vim
Col3a1
Slc2a1
Avpr1a
PC Mid PP PC Mid PP
AvilCre+AAVrg-GFP
AvilCre+AAVrg-taCasp3
d
p-value(-log10)
PERIPORTAL
GO_Biological_Process cotranslational protein targeting to membrane (GO:0006613)
GO_Biological_Process SRP-dependent cotranslational protein targeting to membrane (GO:0006614)
GO_Biological_Process protein targeting to ER (GO:0045047)
GO_Biological_Process cytoplasmic translation (GO:0002181)
GO_Biological_Process cellular protein metabolic process (GO:0044267)
MGI_Mammalian_Phenotype abnormal lipid homeostasis MP:0002118
MGI_Mammalian_Phenotype abnormal liver physiology MP:0000609
MGI_Mammalian_Phenotype hepatic steatosis MP:0002628
Jensen_DISEASES Leigh disease
Jensen_DISEASES Fatty liver disease
MGI_Mammalian_Phenotype abnormal enzyme/coenzyme activity MP:0005584
MGI_Mammalian_Phenotype increased liver weight MP:0002981
MIDLOBULAR
GO_Biological_Process cotranslational protein targeting to membrane (GO:0006613)
GO_Biological_Process SRP-dependent cotranslational protein targeting to membrane (GO:0006614)
GO_Biological_Process protein targeting to ER (GO:0045047)
GO_Biological_Process cytoplasmic translation (GO:0002181)
GO_Biological_Process cellular protein metabolic process (GO:0044267)
MGI_Mammalian_Phenotype abnormal lipid homeostasis MP:0002118
MGI_Mammalian_Phenotype abnormal liver physiology MP:0000609
MGI_Mammalian_Phenotype preweaning lethality, complete penetrance MP:0011100
MGI_Mammalian_Phenotype hepatic steatosis MP:0002628
MGI_Mammalian_Phenotype abnormal hepatocyte morphology MP:0000607
Jensen_DISEASES Leigh disease
Jensen_DISEASES Fatty liver disease
PERICENTRAL
GO_Biological_Process cotranslational protein targeting to membrane (GO:0006613)
GO_Biological_Process SRP-dependent cotranslational protein targeting to membrane (GO:0006614)
GO_Biological_Process cellular protein metabolic process (GO:0044267)
GO_Biological_Process cytoplasmic translation (GO:0002181)
GO_Biological_Process protein targeting to ER (GO:0045047)
MGI_Mammalian_Phenotype abnormal lipid homeostasis MP:0002118
MGI_Mammalian_Phenotype abnormal liver physiology MP:0000609
MGI_Mammalian_Phenotype preweaning lethality, complete penetrance MP:0011100
MGI_Mammalian_Phenotype oxidative stress MP:0003674
MGI_Mammalian_Phenotype abnormal circulating amino acid level MP:0005311
Jensen_DISEASES Leigh disease
Jensen_DISEASES Fatty liver disease

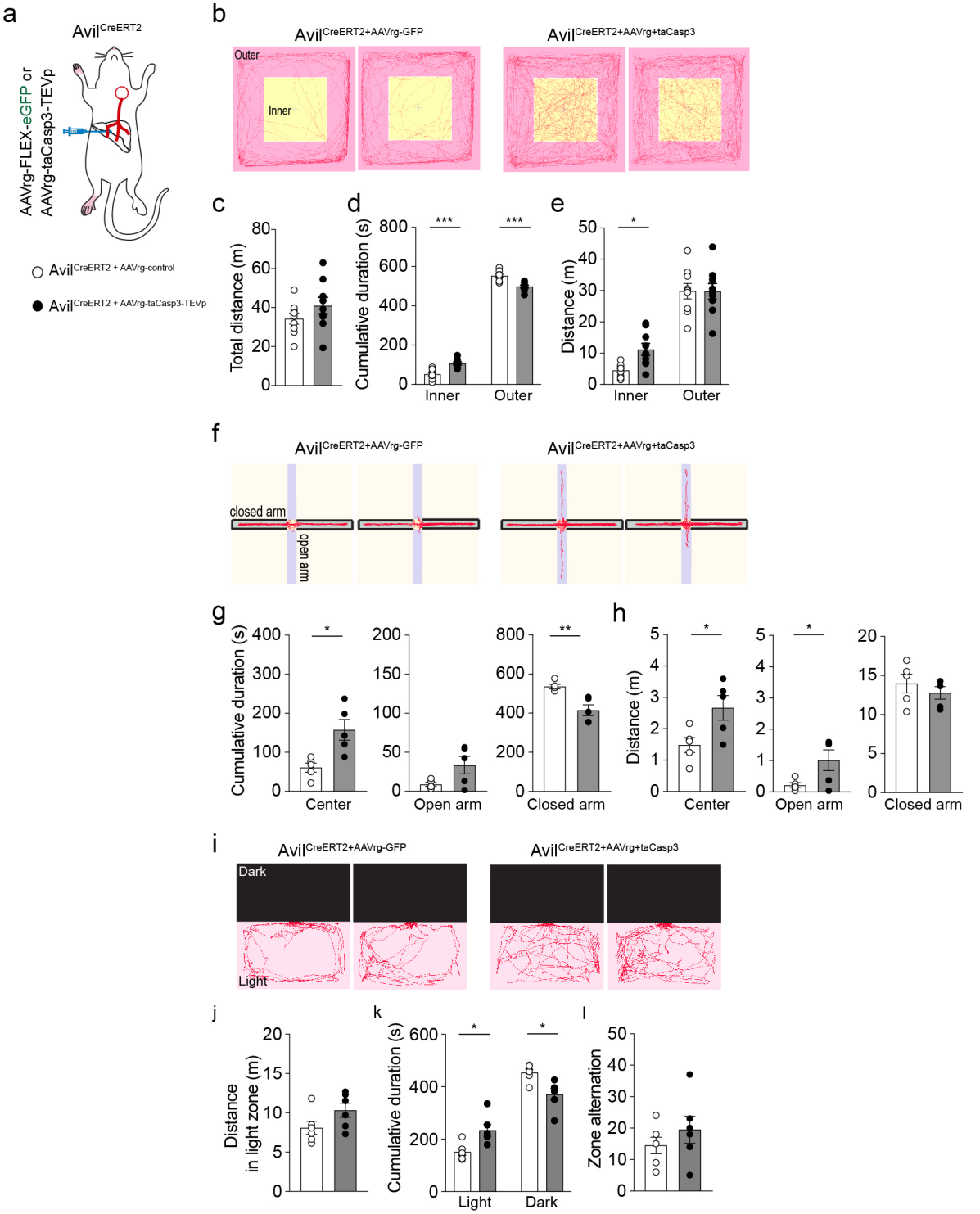
a
AvilCreERT2
AAVrg-FLEX-eGFP or
AAVrg-taCasp3-TEVp
AvilCreERT2 + AAVrg-control
AvilCreERT2 + AAVrg-taCasp3-TEVp
b
AvilCreERT2+AAVrg-GFP
AvilCreERT2+AAVrg+taCasp3
Outer
Inner
c
Total distance (m)
d
Cumulative duration (s)
***
***
Inner
Outer
e
Distance (m)
*
Inner
Outer
f
AvilCreERT2+AAVrg-GFP
AvilCreERT2+AAVrg+taCasp3
closed arm
open arm
g
Cumulative duration (s)
*
**
Center
Open arm
Closed arm
h
Distance (m)
*
*
Center
Open arm
Closed arm
i
AvilCreERT2+AAVrg-GFP
AvilCreERT2+AAVrg+taCasp3
Dark
Light
j
Distance
in light zone (m)
k
Cumulative duration (s)
*
*
Light
Dark
l
Zone alternation